$SnZrCh_3$ materials

2009/2010 report

Andriy Zakutayev

This report consists of 4 sections. It starts with the XPS study of SnZrCh3 pressed pellets, and follows with 3 sections related to thin films in Sn-Zr-Ch system. These 3 thin-film sections report (i) in-situ preparation of Sn-Zr-Ch samples and their ex-situ processing, (ii) preparation of Sn-Zr-Ch samples from Sn/Zr multilayer precursors, and (iii) preparation of Zr-Se and Sn-S thin films.

Section 1. XPS of SnZrCh3 pellets

Experiment

$SnZrS_3$, $SnZrSe_3$, $ZrSe_2$ and SnSe pressed pellets were synthesized from the elemental precursors by reaction in sealed glass ampoules. Precursors for one $SnZrS_3$ sample were grinded before the synthesis in the air and precursors for the other one were grinded in Ar-filled glovebag. All precursors for the Se-based samples were grinded in glove-bag. Some $SnZrSe_3$ pellets were also doped with Sb and Bi up to 5 at. %. The doping was performed by replacing the appropriate amount of Zr for Sb and Sn for Bi in the starting elemental mixture. The pellets were characterized with XRD and EPMA. More experimental details can be found elsewhere.[1,2]

XPS of the pellets was measured in monochromized Al *K*α radiation using Escalab 250 system calibrated with clean Ag sample. Before the measurements the samples were polished with 600-grit SiC sandpaper, inserted into the vacuum that reached 10^{-6} mbar in 10 minutes from grinding. All the peaks observed in survey spectra were due to either photoemission or Auger electrons

from Sn, Zr, S, O and C. There were no Si peaks after polishing the surfaces with SiC sand paper. Surface compositions of the pellets were calculated from the integrated area under the core level peaks taking into account sensitivity factors. Density of states (DOS) of $SnZrCh_3$ was calculated using the general gradient approximation of the density functional theory (GGA DFT), as implemented in the VASP code.

Results and discussion

A. $SnZrS_3$

Composition of $SnZrS_3$ surfaces and resulting atomic ratios measured by XPS are shown in Table I. The samples grinded in Ar atmosphere contain slightly less oxygen than the sample grinded in air, but this difference is comparable to the experimental uncertainty. In both cases Sn/Zr ratio is larger than 1, which is favorable for the $Sn_{1+x}Zr_{1-x}S_3$ phase formation. On the other hand, S/Zr ratio is less than 3, which suggests that extra S has to be added during $SnZrS_3$ synthesis. This is supported by experimental finding that addition of 5 at.% extra S improves the formation of $SnZrS_3$ phase and reduces the amount of ZrSe2 impurity.[2] Overall, the anion/cation ratio is greater than 1.5 due to presence of ~20 at.% of O. Surface oxidation is likely to be the cause of high resistivity of $SnZrS_3$ pressed pellets.[2] The oxide is present mostly on the surface, because surface-sensitive XPS measurements show ~20 at.% of O, and bulk-sensitive EPMA measurements show only 2 at.% of O (Table I). Similarly to the surfaces, the bulk of $SnZrS_3$ is S-poor and has Sn/Zr ratio close to 1.

Core-level spectra of $SnZrS_3$ samples are shown in Fig. 1. Sn, Zr and Ch peaks have high-binding energy shoulders attributed to surface oxidation. Since for Zr peak the ratio of intensities

of the shoulder and the main peak is the largest, Zr-O is likely to be present at the surface. The O peak has two components consistent with hydro-carbon atmospheric contaminants (high binding energy component) and O bound to Zr, S and Sn (low binding energy component)

Table I. Composition and resulting elemental ratios of SnZrS3 pressed pellets measured by XPS and EPMA

at. %	O	Zr	Sn	S	An./Cat.	O/Sn	Sn/Zr	S/Zr
XPS Ar	0.19	0.17	0.18	0.46	1.86	1.08	1.07	2.70
XPS air	0.21	0.16	0.19	0.43	1.79	1.08	1.19	2.63
EPMA air	0.02	0.20	0.22	0.57	1.40	0.08	1.08	2.82

The XPS valence band (VB) spectra and the DFT DOS of $SnZrS_3$ are shown in Fig. 2a. Since the DFT energy reference level is arbitrary, DOS was shifted to align with the measured XPS spectra. The shapes of the XPS spectra and the DFT DOS spectra are in a good agreement with each other, the only difference being the intensity of the Sn 4d peak at ~ 13 eV. In Fig. 2a, the intensity of this peak was divided by 100 for the plotting purpose. The next higher energy peak at ~8 eV is derived from S 3s states. The valence band of $SnZrS_3$ is composed of Sn 5s, Zr 4d and S 3p orbitals, according to the DFT calculation (Fig. 2a).

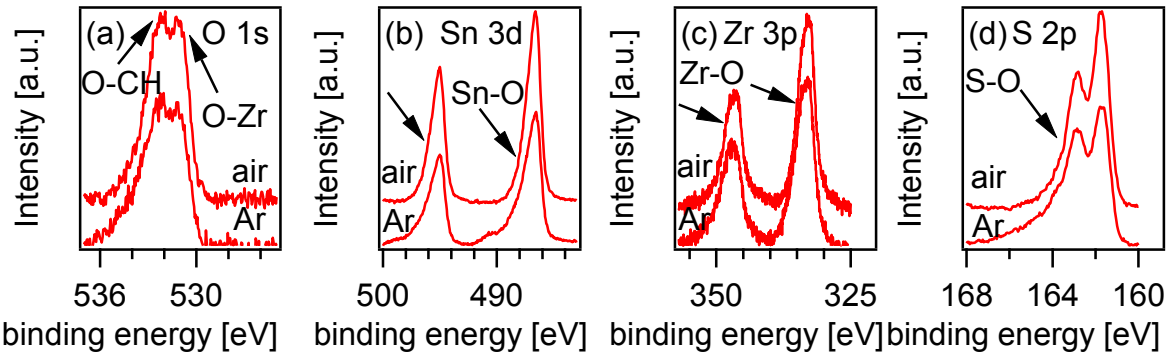

Fig. 1 Core-level spectra of $SnZrS_3$ pressed pellets

Experimental XPS VB binding energy is 1.2 eV, which means that the Fermi level (E_F) at the surface is close the conduction band, since the band gap of $SnZrS_3$ is 1.2-1.4 eV.[1,2] This position of the E_F is rather unexpected, since $SnZrS_3$ has a positive Seebeck coefficient. These observations lead to conclusion that $SnZrS_3$ bands bend down towards the surface, as shown in Fig. 2b. This also indicates that Seebeck effect is not a surface but bulk phenomenon, in constrast to belives of some researchers.[3] Theoretical band gap of $SnZrS_3$ calculated by DFT is 1 eV.

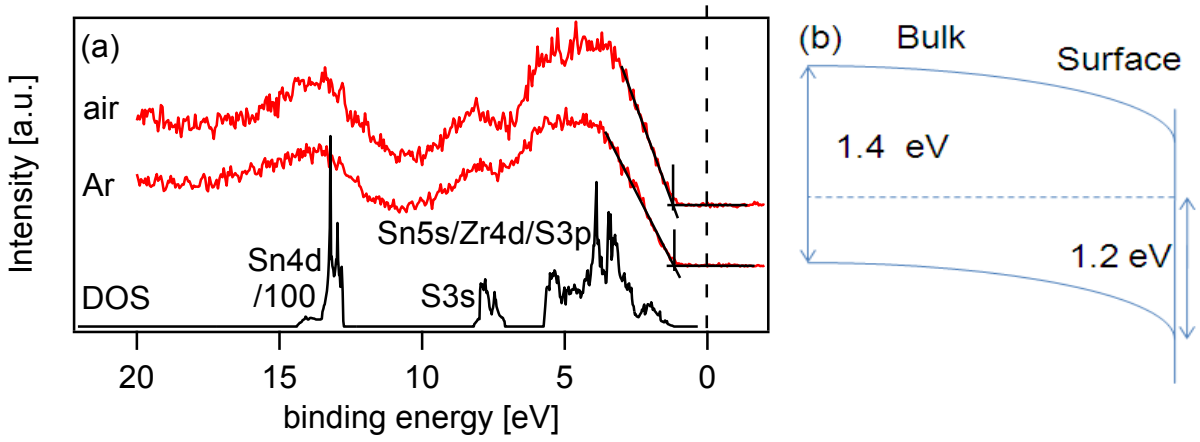

Fig. 2 (a) SnZrS3 valence band spectra and DFT density of states calculated by Wien and VASP programs. DOS below ~10 eV is divided by 100 for scaling. (b) SnZrS3 surface band bending

B. $SnZrSe_3$

$SnZrSe_3$ pellets were doped with 2%- and 5% Bi and Sb to investigate the effect of the doping on the Fermi level. Bi was intended to substitute for Zr and Sb was intended to replace Sn, so the precursor mixtures were poor by the corresponding amounts of Sn and Zr.

Fig. 3 shows the XPS core level spectra of $SnZrSe_3$. Core level spectra of the pure and doped $SnZrSe_3$ samples are similar to each other and also resemble the $SnZrS_3$ core level spectra (Fig. 2) As shown in Fig, 3b, degree of the oxidation of Sn in $SnZrSe_3$ samples is random between different pellets, so the difference most likely comes from non-uniformities due to the surface polishing. On the other hand, Zr is oxidized consistently to the same degree for all the samples (Fig. 3c), which points to the oxidation during or after the synthesis. The ratio of intensities of Se $3d_{5/2}$ and Se $3d_{3/2}$ peaks is not consistent with the electron population of the corresponding electron shells (Fig. 3d). This means there is a large high-binding energy component in the Se core level spectrum, most likely caused by Se-O. The O 1s peak itself has two components, similar to that in $SnZrS_3$ spectra.

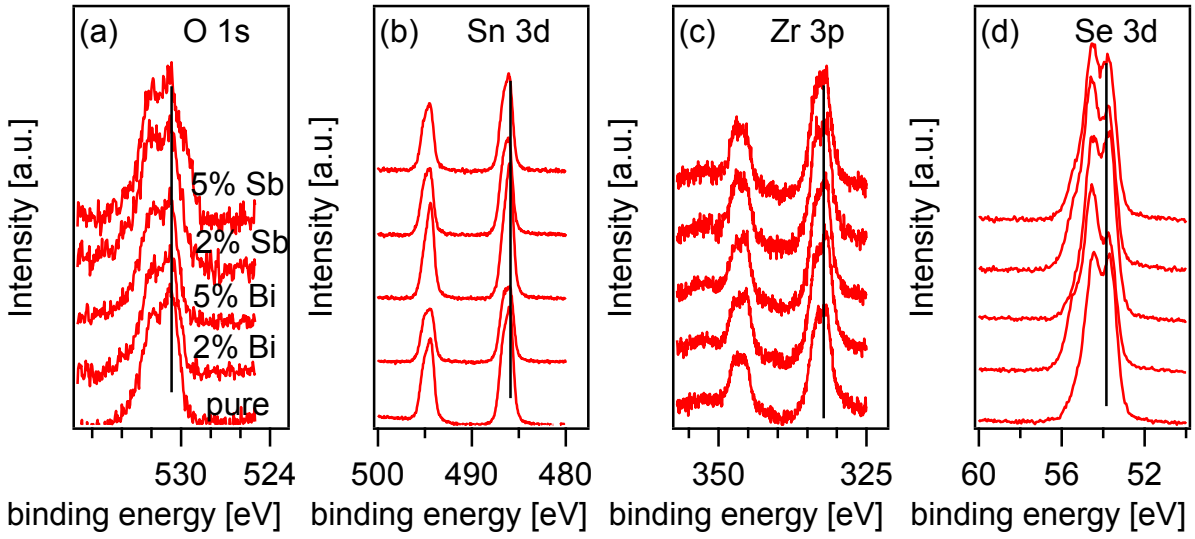

Fig. 3 Core-level spectra of $SnZrSe_3$ pressed pellets. The doping levels in (a) are the same for all the spectra in a row.

Doping leads to incorporation of Sb and Bi in $SnZrSe_3$ structure. Core level spectra of these elements were obtained by subtracting the core level spectra of the undoped sample from those

of the doped samples and are shown in Fig. 4a and 4b. At 5% doping level the peaks are clearly evident, but for 2% doped samples their presence is less clear. Regardless of the dopand type (Bi or Sb) and concentration (2% or 5%), the valence band binding energy remains fixed at 0.65 eV, which points to the pinning of the Fermi level at the surface (Fig. 4c). The pinning of E_F is also evident from the constant binding energies of the XPS core level spectra (Fig. 3). Position of the surface Fermi level should be close to the CB, since the estimated experimental band gap of $SnZrSe_3$ (0.8 eV) is comparable to the valence band binding energy (0.65 eV). The $SnZrSe_3$ VB spectra measured by XPS favorably agree with the calculated DFT density of states. According to the DFT calculations, the valence band character of $SnZrSe_3$ down to BE=20 eV is similar to that of $SnZrS_3$, except S 3s and 3p peaks are replaced with Se 4s and 4p peaks (Fig. 4c). Theoretical band gap of $SnZrSe_3$ calculated by DFT is 0.5 eV.

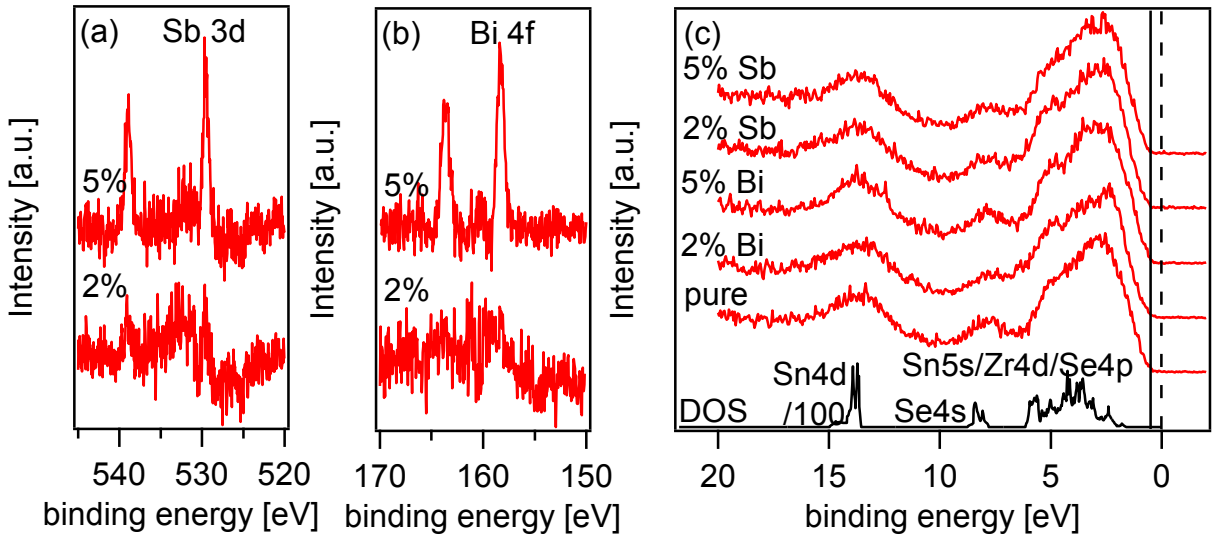

Fig. 4 XPS spectra of (a, b) the dopand core levels and (c) SnZrSe3 valence band and DOS. DOS below ~10 eV is divided by 100.

Surface composition of $SnZrSe_3$ samples is summarized in Table 3. In all samples Se/(Zr+Sb) ratio is consistently larger than 3, so all the surfaces are Se-rich. Bi/(Sn+Bi) and Sb/(Zr+Sb) ratios are consistent with the intended doping levels, within the accuracy of this experimental technique. On the other hand, the (Sn+Bi)/(Zr+Sb) ratio varies considerably which was not observed in $SnZrS_3$ pellets. This indicates that the synthesis process has to be controlled better to achieve appropriate stoichiometry. O/Zr ratio is close to 2, which points to the presence of ZrO_2 at the surface. This is consistent with the shape of Zr 3p core level peaks (Fig. 3c). Additional evidence for oxidation of the surfaces is the anion/cation ratio being larger than 1.5.

Table II. Composition and resulting elemental ratios of SnZrSe3 pressed pellets measured by XPS

at. %	Sn +Bi	Zr +Sb	Se	O	(Sn+Bi)/ (Zr+Sb)	an./ cat.	Se/ (Zr+Sb)	O/ (Zr+Sb)	Sb/ (Zr+S)	Bi/ (Sn+Bi)
pure	0.20	0.12	0.44	0.24	1.59	2.13	3.56	1.94	0.00	0.00
2%Bi	0.14	0.16	0.47	0.23	0.87	2.41	3.00	1.49	0.00	0.03
5%Bi	0.18	0.13	0.45	0.23	1.42	2.19	3.49	1.79	0.00	0.03
2%Sb	0.14	0.14	0.43	0.29	0.94	2.58	3.01	2.00	0.03	0.00
5%Sb	0.14	0.14	0.43	0.29	1.05	2.54	3.10	2.11	0.06	0.00

C. $ZrSe_2$ and SnSe

$SnZrSe_3$ can be viewed to have two parent materials, SnSe and $ZrSe_2$. In $SnZrSe_3$, these two materials are combined in a way to form a structure similar to that of not thermodynamically stable Sn_2Se_3.Because of these relationships, photoemission spectra of SnSe and $ZrSe_2$ were studied and compared to that of undoped $SnZrSe_3$.

Core level spectra of SnSe, $SnZrSe_3$ and $ZrSe_2$ are shown in Fig. 5. The degree of the surface oxidation decreases in the SnSe-SnZrSe3-$ZrSe_2$ order (Fig. 5a), as expected from the reactivity of the constituent elements with oxygen. Zr peaks in $ZrSe_2$ and $SnZrSe_3$ have similar high-binding energy shoulders related to oxidation (Fig. 5c). Se peak or $ZrSe_2$ also has an intense oxide shoulder which may be related to replacement of some Se atoms with O due to weak Se-Se bonds in this material (Fig. 5d). Se peak in SnSe has an expected shape for a 3d level. Sn peak in SnSe has a smaller high-binding-energy shoulder compared to the Sn peak in $SnZrSe_3$.

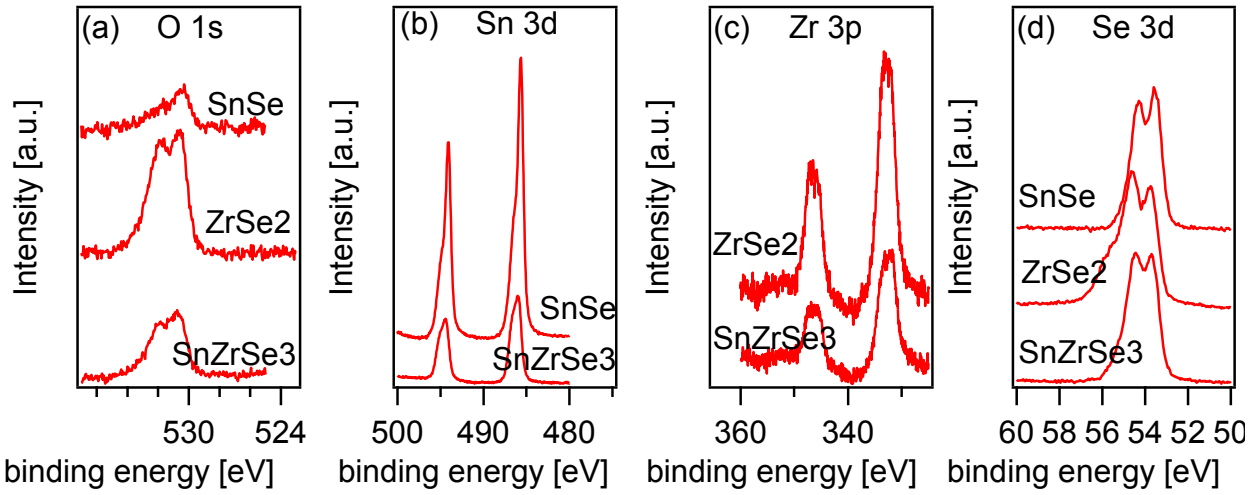

Fig. 5 Core-level spectra of SnSe, $ZrSe_2$ and $SnZrSe_3$ pressed pellets.

Surface composition of SnSe and $ZrSe_2$ determined from the XPS spectra and bulk composition measured using EPMA are summarized in Table III. SnSe surface is slightly Se-poor compared to the bulk and has similar oxygen content as bulk of the sample. This points to incorporation of oxygen in the grains during the synthesis. On the other hand, $ZrSe_2$ surface is significantly more Se-poor and more oxidized than the bulk, which indicates predominantly surface location of the oxide. O/Zr ratio on the surface of $ZrSe_2$ (Table III) and $SnZrSe_3$ (Table II) are similar.

Table III. Composition and resulting elemental ratios of ZrSe2 and SnSe measured by XPS and EPMA

at. %	Metal	Se	O	Se/Metal	(Se+O)/Metal	Se/O	O/Metal
SnSe XPS	0.47	0.38	0.15	0.80	1.13	2.43	0.33
ZrSe2 XPS	0.22	0.39	0.39	1.81	3.60	1.01	1.80
SnSe EPMA	0.44	0.42	0.13	0.95	1.25	3.17	0.30
ZrSe2 EPMA	0.29	0.60	0.11	2.04	2.40	5.67	0.36

The valence band spectra of the three materials are compared in Fig. 6a. The valence band binding energy increases in the SnSe-$SnZrSe_3$-$ZrSe_2$ series. As shown in Fig. 6 (b and c), the Fermi level at the SnSe surface is closer to the VB, whereas it is closer to the CB on the $ZrSe_2$ surface. This is consistent with p- and n-type conductivity of these two materials. For SnZrSe3, the Fermi level is closer to the CB, than to the VB. This contradicts with the measured positive Seebeck coefficient of $SnZrSe_3$, in a similar way as was discussed for $SnZrS_3$.

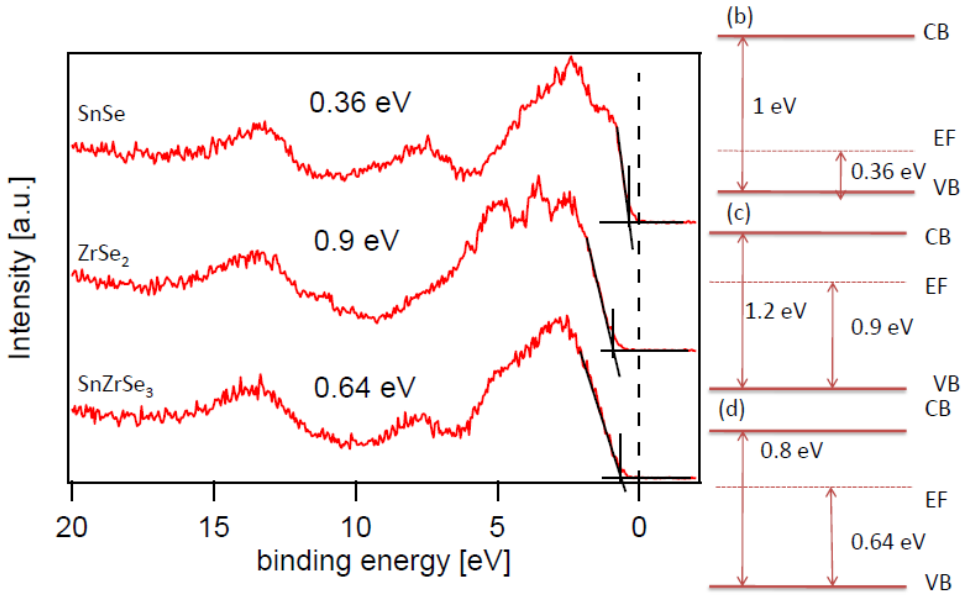

Fig. 6 (a) Valence band spectra of SnSe, $ZrSe_2$ and $SnZrSe_3$. Band diagrams of (b) SnSe, (c) $ZrSe_2$, and (d) $SnZrSe_3$

Summary

XPS study of $SnZrSe_3$ pressed pellets shows that the position of the Fermi level at the surface does not depend on the doping type and concentration. This is attributed to oxidation if the surfaces of the samples, similar to that in $ZrSe_2$. In SnSe, on the other hand, the degree of oxidation is much smaller, therefore Sn-Ch materials system may have better surface properties. The bands of $SnZrCh_3$ bend down towards the surface, based on the results of the XPS and Seebeck effect measurements. The XPS valence band spectra of both $SnZrCh_3$ materials agree with the results of the DFT DOS calculation. According to DFT, the valence band is derived from Sn 5s, Zr 4d and Ch np states (n=3 for S, n=4 for Se). Overall, $SnZrSe_3$ surface properties are more similar to those of $ZrSe_2$ rather than SnSe.

Section 2. Sn-Zr-Ch thin films from $SnZrCh_3$ targets

Experiment

Sn-Zr-Ch (Ch = S, Se) films were prepared by PLD in the Thermionics chamber with 10^{-9} Torr base pressure. The pressure in the chamber increased to 10^{-7} – 10^{-6} Torr during the ablation of the $SnZrCh_3$ targets and when the substrate was heated (up to 700^{o}C). Before the deposition, the substrates were cleaned in methanol and deionized water. Right after the deposition the samples were quickly (~100 ^{o}C/min) cooled to room temperature by turning off the heater. Some of the samples were cooled in a controlled way at 10 ^{o}C/min.

Deposition parameters were varied to study the transport of element from the target to the substrate. Studied parameters included substrate temperature, pressure of the gas in the chamber (100 % Ar, 95% Ar / 5% H_2), type of the gas, target-substrate distance, laser beam intensity, laser repetition rate, type of the substrate (SiO_2, Si), and type of a target (single phase, SnCh-rich, mixed binary phase). *Ex-situ* processing techniques were also applied to the samples prepared by PLD. This post-processing methods included sealed-tube anneal (STA) also referred to as chalcogen vapor anneal (CVA), H_2Ch flowing gas anneal and rapid thermal anneal (RTA). The resulting samples were studied using XRD and EPMA.

Results and discussion

The films deposited from stoichiometric $SnZrCh_3$ targets are always Sn- and Ch-poor. Since the target are composed of stoichiomteric $SnZrCh_3$, possible reasons of non-stoichiometry of the

films are (i) modification of the target during PLD, (ii) scattering on the way from to the subsrtate (mass transfer coefficient of Ar/S should be large due to similar masses), different sticking coefficients, re-evaporation and re-sputtering rates of Sn, Zr and Ch. Modification of the target was excluded from this list of the possible reasons by EPMA study.[1] Deviation of the films from the $SnZrCh_3$ composition lead to detailed investigation of various deposition conditions on the stoichiometry and phase of the samples.

A. Main deposition variables: Sn-Zr-S

Atomic ratios in the Sn-Zr-S films prepared by PLD are shown in Fig. w. Above 500oC, significant loss of Sn and Ch is observed (Fig. 7a). We attribute this loss to increasing rate of evaporation of Sn-S-containing phases from the substrate in this temperature region. In general, we believe that one of the reasons for difficulty in producing $SnZrCh_3$ phase is the contrast of low melting points of Sn and S and refractory nature of Zr. Another reason related to it is the weak Sn-Ch bonds in $SnZrCh_3$ structure.[1] Weak bonds must lead to high equilibrium vapor pressure of Sn and Ch above growing Sn-Zr-Ch thin film and consecutive loss of these elements.

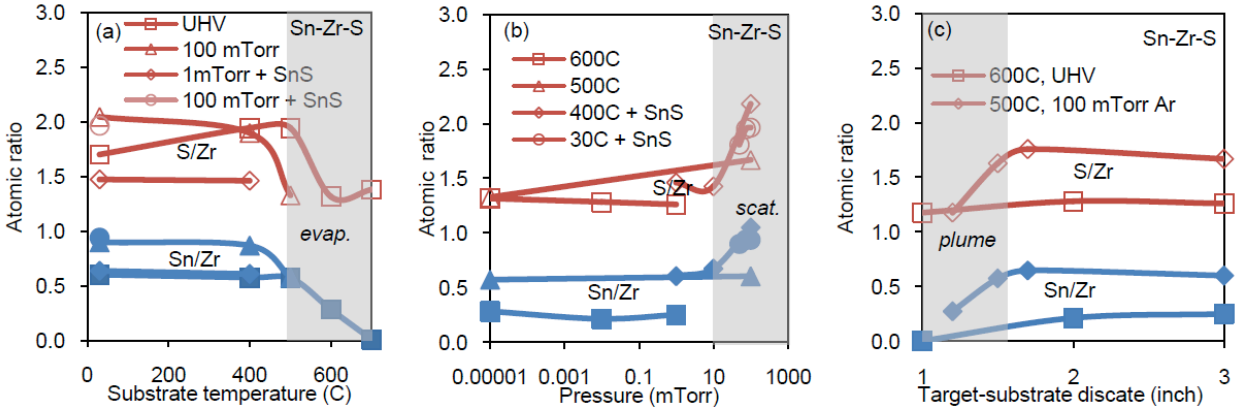

Fig. 7 Sn/Zr (closed symbols) and S/Zr (open symbols) atomic ratios in the films on SiO2, as a function of (a) substrate temperature, (b) Ar pressure, and (c) target-substrate distance

Below 500 ^{o}C, Sn- and S-content depends on the Ar pressure in the chamber during the deposition. Increase of the Ar pressure above 10 mTorr, increases Sn/Zr and S/Zr ratios in the thin films (Fig. 7b). This trend correlates with the change in the deposition regime in this pressure range. This change is also manifested by brightening and rounding of the plume. Brightening and rounding are associated with multiple scattering events of the ablated species on the Ar atoms present in the chamber. In literature this phenomenon is described as a transition from the molecular flow (< 10 mTorr) to the referred to as viscous flow (>100 mTorr) regime.[4]

Sn and S content of the film largely depends on the target-substrate distance in a viscous flow regime (Fig. 7c). Sn and S content starts decreasing when the substrate is positioned inside of the plume. This is also observed for the deposition in the molecular flow regime (up to 10 mTorr), but the effect is not so dramatic, because the plume is larger and more smeared in this pressure range. Decrease of the Sn and S content with decreasing target-substrate distance can be attributed to re-sputtering of these volatile species by incident particles and by additional heating of the substrate by hot plume.

Some of the Sn-Zr-S samples were deposited from the SnZrS3 target with 5 at.% extra SnS (Fig. 7). These samples show somewhat larger Sn/Zr ratio, but S/Zr ratio is essentially the same, which indicates that the S atomic content is dependent on the Sn and Zr concentrations in the sample.

B. Main deposition variables: Sn-Zr-Se

Deposition of Sn-Zr-Se thin films on Si substrates allowed determination of the oxygen content of the samples by EPMA. The effect of the Si native oxide (~5 nm) on EPMA results is small and can be accounted for.

Dependence of the Sn/Zr and Se/Zr ratios on the substrate temperature (Fig. 8a) is similar to that in Sn-Zr-S samples. Sn- and Se content are stable up until ~200 oC, when melting of these elements occurs. Sn/Zr and Se/Zr ratios fluctuate up until 600 oC. Above this temperature, even less Sn and Se are detected in the films. On the other hand, O/Zr ratio stays constant below 0.5 across the entire investigated temperature range. High reactivity of Zr with O is believed to be an important reason for encountered difficulties in preparation of $SnZrCh_3$ thin films.

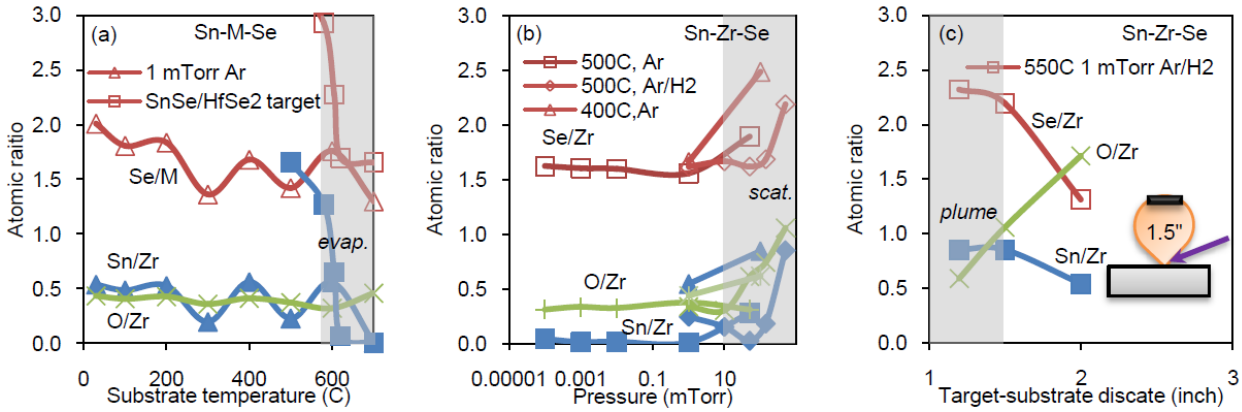

Fig. 8 Sn/Zr (closed symbols), Se/Zr (open symbols), and O/Zr (crossed symbols) atomic ratios in the films on Si, as a function of (a) substrate temperature, (b) gas pressure, and (c) target-substrate distance. Inset (c): schematic position of the substrate on the edge of a plume

We also used $SnSe/MSe_2/In_2Se_3$ (M = Zr, Hf) mixed binary phase targets in attempt to prepare $SnMCh_3$ films in ultra-high vacuum. The components were mixed in the rations 50/50/5 at. % and cold-pressed. The plume for these deposition runs looked non-uniform, namely bright sparks

in the plume were observed. For the samples prepared from this target, similar dependence on the substrate temperature is observed (Fig. 8a). The transition to Sn-poor samples happens in the vicinity of 600 oC which coincides with the phase transition of orthorhombic to tetragonal SnSe. The samples prepared below 550^{o}C have quite high Sn- and Se content, but Se/(Sn+Hf) ratio is smaller than 3/2, so the desired phases did not form. It is likely that better result may be reached by using $SnSe_2/MSe_2$ mixed phase targets with smaller Sn/Zr ratios.

Sn-Zr-Se samples were deposited in Ar and Ar/H_2 atmospheres (Fig. 8b). For Ar gas, Sn/Zr and Se/Zr ratio show similar dependence on the pressure as in the case of Sn-Zr-S, increasing above 10 mTorr. On the other hand, the Sn- and Se content of the samples prepared in Ar/H_2 atmosphere dip at ~50 mTorr and only then start increasing. This difference must be related to the reactivity of hydrogen species in Ar/H_2 gas.

The target-substrate dependence of the Sn- and Se content of the Sn-Zr-Se samples deposited in Ar/H_2 gas is opposite to that of Sn- and S content of Sn-Zr-S samples deposited in pure Ar (Fig. 8c). Sn/Zr and Se/Zr ratios decrease significantly when the substrate is positioned outside of the plume. Se/Zr drop is especially dramatic, which indicates the reaction process between selenium and hydrogen in the plume. In the case if the substrate is positioned in the plume, Se- and Sn content remain relatively high (Fig. 8c, inset). It is also possible that the difference in the effect of the target-substrate distance on the composition of Sn-Zr-S and Sn-Zr-Se samples is caused by different chalcogen atoms, rather than the difference in the gas. However, this is not likely because of the similar dependence of Sn-Zr-S and Sn-Zr-Se on the main and the other deposition conditions.

Important question is the origin of oxidation of the Sn-Zr-Ch samples. We believe that most of the oxygen is absorbed into as-prepared chalcogen-poor thin film samples when they are exposed to the atmosphere. Some oxygen atoms must be also incorporated into the sample during the deposition, since the $SnZrSe_3$ target contains some oxygen.[1]

C. Other deposition conditions: Sn-Zr-Ch

Sn/Zr and S/Zr ratio increase with increasing laser beam intensity (Fig. 9a). This may be attributed to the transfer of larger amount of material from the target to the substrate which balances the re-evaporation at 600°C substrate temperature. The upper limit of the laser beam intensity is imposed by the target density: at 3 J/cm^2 the surface of the target contained small craters.

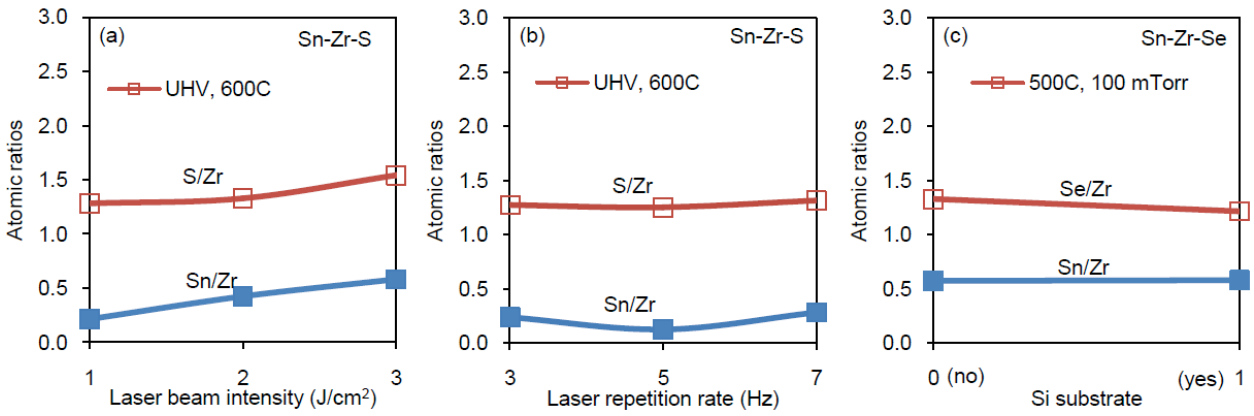

Fig. 9 Sn/Zr (closed symbols), Se/Zr (open symbols) atomic ratios as a function of (a) laser beam intensity, (b) laser repetition rate, and (c) type of a substrate.

Laser repetition rate and type of the substrate do not significantly influence the Sn- and Ch content. Observed variation with repetition rate can be attributed to the compositional

fluctuations low stability of the sample at 600°C substrate temperature (Fig. 9b). Variation with the type of a substrate may be also explained by the temperature difference on the surface of the substrates – the samples on a-SiO_2 and Si substrates were deposited in the same run, and the temperature calibration for these substrates differs by ~50 °C. (Fig. 9c)

D. Spatial variation of content in Sn-Zr-Se thin films

Sn-Zr-Se samples were studied for the uniformity of the composition across the substrate. For these experiments, thin films were deposited in 1 mTorr of Ar on 1"x1" Si substrate held at room temperature without rotation (Fig. 10). Overall, observed variation of Sn/Zr and Se/Zr ratios are relatively small on the scale of the shadow mask size used for the other experiments (~5x5 mm), and the O/Zr ratio stays constant across the entire sample. The sidewise variation of Sn/Zr and Se/Zr (Fig. 10c) is larger than the front-back variation (Fig. 10a and 10b), in contrast to $LaAlO_3$ where most of the variation is observed in the forward-backward direction. Overall, spatial variation in the composition of Sn-Zr-Se samples is smaller than for $LaAlO_3$.[5]

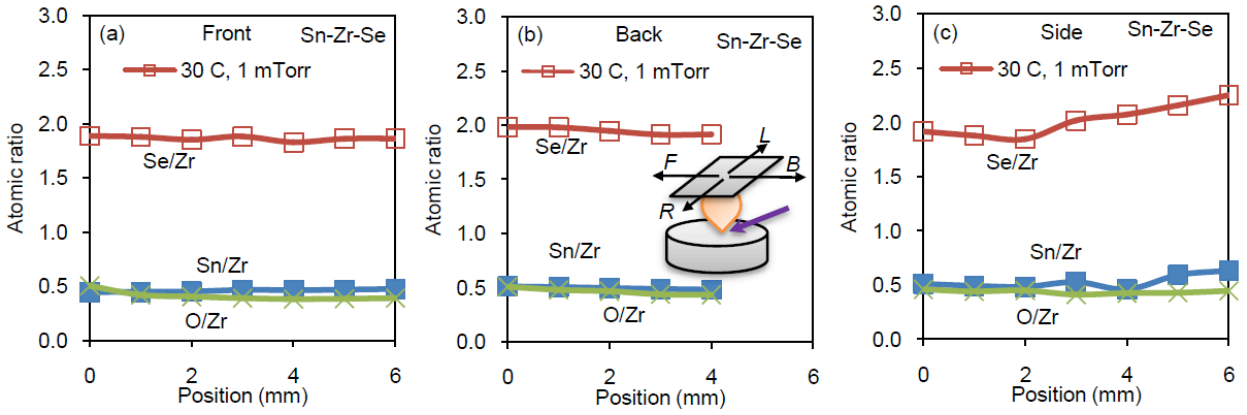

Fig. 10 Spatial variation of the Sn-Zr-Se sample content in (a) front, (b) back, and (c) side directions, with respect to the incidence direction of the beam. Inset (b): schematic drawing of the directions

E. Phase identification

All the samples reported above were characterized by x-ray diffraction (XRD). As-deposited Sn-Zr-Ch samples rarely showed XRD peaks of the $SnZrCh_3$ phases, and if they did, the peaks were very weak compared to the peaks of the binary phases. Below we show several representative XRD patterns of Sn-Zr-Ch samples prepared *in-situ*.

Sn-Zr-S samples deposited at 400°C consist mainly of Sn, ZrS and ZrS_2 phases (Fig. 11a). Intensity of Sn peaks increases and intensity of ZrS_x peals decreased with increasing Ar pressure, in agreement with EPMA results. For the Sn-Zr-Se samples the main phases were Sn, $ZrSe_2$ and $Zr_{3.75}Se_6$ (Fig. 11b). $ZrSe_x$ phases are dominant at 600°C, Sn phase dominates at 400°C, and the sample is amorphous below 200°C.

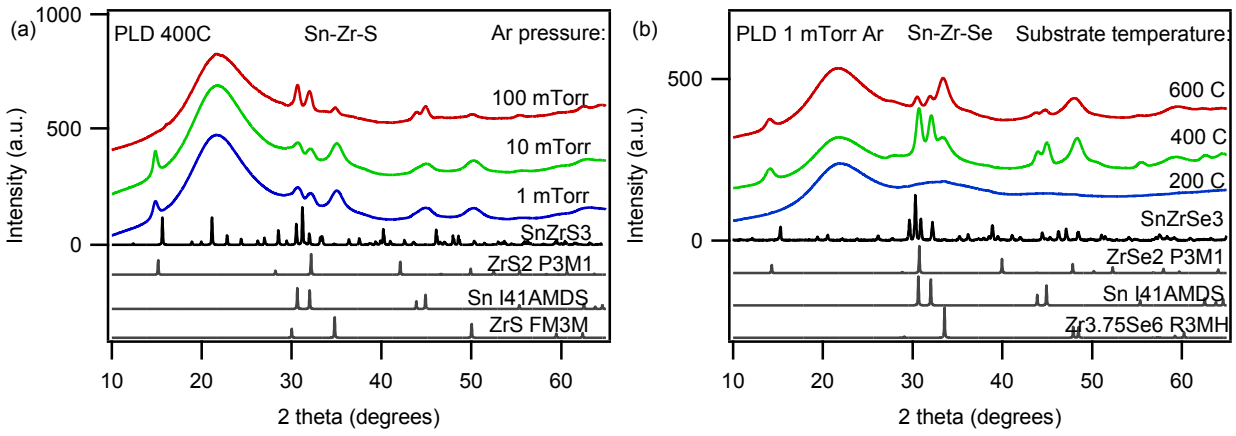

Fig. 11 Typical XRD patterns of (a) Sn-Zr-S, and (b) Sn-Zr-Se thin films on SiO_2 in Ar atmosphere.

F. Post-processing of Sn-Zr-Ch samples

Ex-situ processing by sealed tube anneal and somewhat improved the stoichiometry and phase composition of the samples. On the other hand, flowing H_2S gas anneals and RTA resulted in oxygen incorporation and did not led to formation of $SnZrCh_3$ phase.

Post-processing of the Sn-Zr-S samples by sealed tube anneal at 700°C produced the samples with majority $SnZrS_3$ phase (Fig. 12a). The starting samples for this study were prepared by PLD in UHV at room temperature, so they were somewhat Sn-poor with respect to Zr content. Improvement of the phase content of the samples after the sealed tube anneal correlates with increase of the chalcogen content, as shown by EPMA (Fig. 13a). Unfortunately, transport properties of $SnZrS_3$ films could not be measured. High resistivity of the samples is attributed to the presence of ZrS_x and ZrO_y impurities.

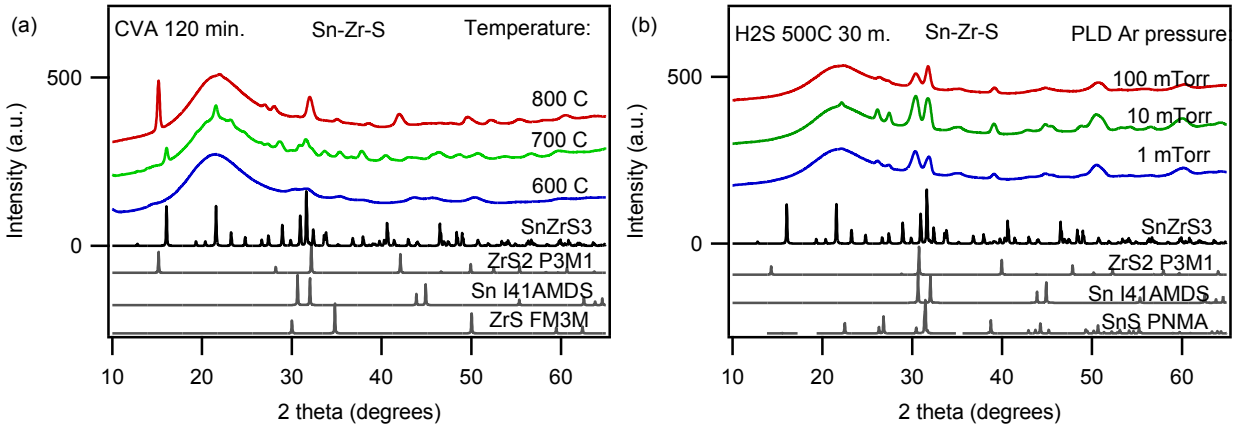

Fig. 12 Typical XRD patterns of Sn-Zr-S thin films post-treated by (a) sealed-tube anneal, and (b) flowing H2S anneal

Flowing gas anneals were less successful in producing $SnZrS_3$ phase. (Fig. 12b). The 3 samples in Fig. 12b were produced in a single H_2S anneal run from 3 Sn-Zr-S samples prepared at different Ar pressure (Fig. 11a). SnS appears in the samples prepared this way, in addition to ZrS_x and Sn. The ratio of two dominant Sn peaks for the sample deposited in 100 mTorr and annealed in H_2S is not consistent with Sn reference pattern. This may point to the presence of small amount of $SnZrS_3$ phase, which also has the strongest peak in this region. As indicated by the results of the sealed tube anneals, larger processing temperatures (~700°C) would be more beneficial for the formation of $SnZrS_3$ phase. However, even at 500°C annealed films contained significant larger amount of oxygen compared to as-deposited samples, as shown by EPMA (Fig. 13b). This amount is expected to increase even more above 600°C, as shown by the results of H_2S anneals of Sn/Zr multilayers.

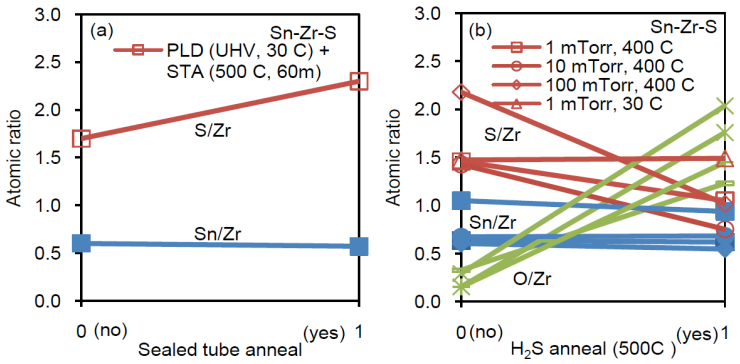

Fig. 13 Sn/Zr (closed symbols), S/Zr (open symbols), and O/Zr (crossed symbols) atomic ratios in the films before and after anneal (a) in a sealed tube, and (b) under flowing H2S gas.

Rapid thermal anneal of the Sn-Zr-S and Sn-Zr-Se samples in flowing Ar in 300-500°C temperature range also did not produce $SnZrCh_3$ phase. The samples had similar phase

composition to those annealed under flowing H_2S (Fig. 12b). This may is attributed mainly to low Ch content of the starting samples, but also may be related to the low used temperature.

Summary and outlook

Sn and Ch atoms do not reach the substrate or leave it during $SnZrCh_3$ ablation. Substrate temperature, gas pressure and type, and target-substrate distance were found to be the most important deposition conditions for control of Sn- and Ch content of the samples. The films were quite uniform over the entire area of the substrate. As deposited films consisted primarily of $ZrCh_x$ and Sn phases. Sn- and Ch- content can be controlled *in-situ* by addition of extra $SnCh_x$ to the target and varying PLD parameters. In addition, $SnZrCh_3$ phase may be achieved by sealed tube anneal of the films with $SnZrCh_3$ powder. H_2S flowing increased the oxygen content of the samples and did not produced the desired phase, RTA was also not successful. Alternative way for in-situ deposition of $SnZrCh_3$ thin films may be co-evaporation of S and Se during the growth. This will provide an additional flux of chalcogen to the substrate and improve the stoichiometry of the films, but should be used with caution to not break the turbomolecular pumps. Overall, difficulty controlling the stoichiometry of the Sn-Zr-Ch system is attributed to the large difference in the melting points of Sn and Zr, weak Ch bonds in $SnZrCh_3$ structure, and high reactivity of Zr with O.

Section 3. H_2Ch anneals of Sn/Zr multilayers

Introduction

One of the ways to prepare thin films of complex chalcogenide absorber materials for solar cells is to deposit metals or binaries and sulfurize or selenize them under flowing H_2S or H_2Se gases respectively. This technique has been proven to produce Cu_2ZnSnS_4 layers for CZTS solar cells with 6% conversion efficiency.[6] It has been shown that after the flowing gas process, the sample prepared from metal multilayer precursors yield higher conversion efficiencies than those prepared from metal stacks. Binary precursors give higher efficiencies than metal multilayers. In the case of a precursor stacks (as opposed to multilayers), the stoichiometry of the final product depends on the order of the precursors and affects the conversion efficiency of the PV devices. Other thin film solar cell absorbers, such as $Cu(InGa)Se_2$ and chalcogenide p-type transparent conductors, such as Cu_3TaS_4 [7] have also been prepared by H_2Ch anneals of metal multilayers.

Experiment

In attempt to prepare $SnZrCh_3$ thin films, Sn/Zr multilayers were deposited by PLD on cleaned Si (001) and a-SiO_2 substrates held at room temperature. Sn- and Zr-metal targets were pre-polished with sand paper and pre-ablated in vacuum chamber with 10^{-5} - 10^{-6} Torr residual pressure. Pulsed laser beam with the energy density of 2 J/cm^2 and repetition rate of 10 Hz was used to ablate the targets, separated from the substrates by ~7 cm. For a few runs, 100 mTorr of 95% Ar / 5% H_2 gas was introduced into the chamber to test its impact on the deposition process. Deposition at elevated temperatures, which enhances the mixing between the multilayers was not considered because of the low melting point of Sn-metal.

The multilayers with 200 Sn/Zr periods were deposited. Each period consisted of 100 laser pulses. Within each period, the ratio of the pulses in Sn- and Zr-targets was varied to change the Sn/Zr atomic ratio in the sample. Preliminary, Sn and Zr deposition rates were calibrated by thickness measurement of thick Sn and Zr films, but this calibration was not accurate, probably due to different Sn/Sn and Sn/Zr deposition rates.

Deposited multilayers were annealed in a tube furnaces under the flow of H_2S gas. Before and after each anneal, the tube was purged for 2h with welding-grade Ar to get rid of atmospheric oxygen (before the anneal) and to get rid to H_2Ch (after the anneal). The samples were heated and cooled with the 10 ^oC/min rate. The three main studied variables were Sn/Zr starting ratio, the temperature and the time of the anneal. The effect of other factors, such as flowing gas rate, flowing gas type (H_2Se), multi-stage temperature protocols, presence of Zr getter, quality of the furnace seal (number of o-rings), the furnace itself (Gilbert 011 or 18) were also studied in some experiments. The samples were investigated by optical microscopy, XRD and EPMA.

Results and discussion

When deposition begins, the pressure inside of the chamber starts to decrease. This trend is opposite to what is usually observed in PLD. We attribute this difference to gettering effect of Zr. Hot Zr atoms in the plasma bind to residual gasses and deposit on the substrate in a solid state, thereby decreasing the gas pressure in the chamber. Another interesting effect during the deposition was emission of Zr particulates from the target after ~5000 laser pulses. These particulates appear to the eye as sparks. Similar effect was noticed for Ta-metal targets during Cu/Ta multilayer deposition.[7] We attribute the “sparking” effect to presence of sharp features on the surface of the refractory metal target, modified by a laser beam. Sparking effect was not

observed for the Sn target, due to its low melting point (232 ^{o}C) and absence of sharp features on the surface.

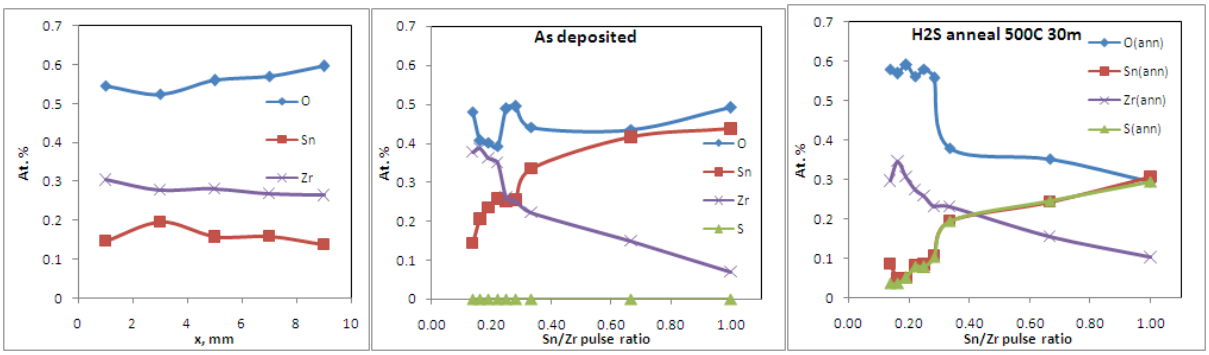

Fig.14 Spatial variation (a) and elemental content of the samples before (b) and after (c) the anneal at 500 ^{o}C for 30 m.

Elemental content of as-deposited samples and its spatial variation for one of the samples are shown in Fig. 14. As shown in Fig. 14b, for as-deposited multilayers, Sn/Zr ratio increases with increasing number of laser pulses in Sn target. Sn and Zr content of the films is equal at the Sn/Zr pulse ratio of 0.28 (22 pulses in the Sn target and 78 pulses in Zr target). All as-deposited sample contain 40-50 at.% of oxygen. The multilayers deposited in Ar/H_2 atmosphere contained even more oxygen. XRD analysis revealed that as-deposited samples are composed of polycrystalline Sn and an amorphous phase, most likely Zr-O. These results are consistent with the optical images of the surfaces of Sn and Zr films: Sn films look grainy, and Zr-O films look smooth (Fig. 15).

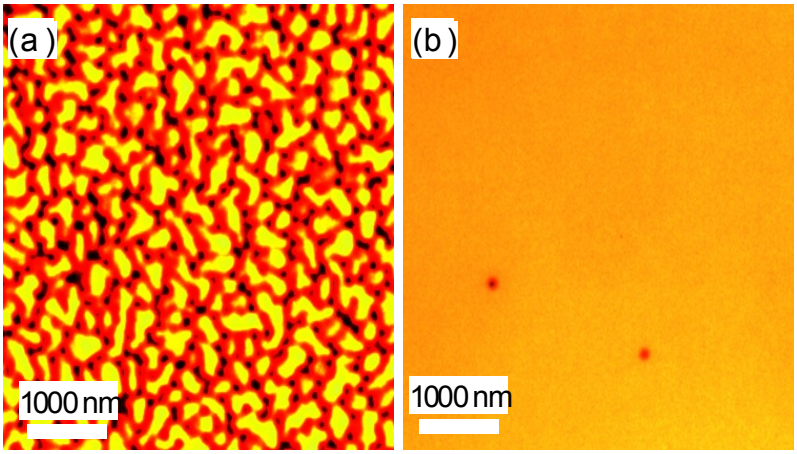

Fig. 15 Optical microscopy images of (a) Sn and (b) Zr thin films prepared by PLD

The Sn and Zr content of the multilayers vary by ~5 at.% in ~10 mm (Fig. 14a). This variation may be explained by different ablation efficiency at 2 J/cm^2 and therefore different geometries of the plume during the deposition.

Annealed samples show similar trend of atomic content as a function of Sn/Zr PLD pulse ratio (Fig. 14c), but there are some differences. One important difference is in the point at which Sn and Zr atomic content are equal (0.45 pulse ration as opposed to 0.28 in as-deposited samples). This indicates that part of Sn is being lost in the sulfurization process. Another difference is that annealed samples contain sulfur, whereas as-deposited thin films do not contain this element.

XRD patterns of the sulfurized Sn/Zr samples are shown in Fig.16. For all Sn/Zr ratios the films are composed of SnS and ZrO_2 phases. The relative intensity of the peaks that correspond to these two materials change as the Sn/Zr ratio in the film changes. Neither of the diffraction peaks could be identified with SnZrS3 phase. XRD patterns of the annealed Sn and Zr layers are also shown in Fig. 16.

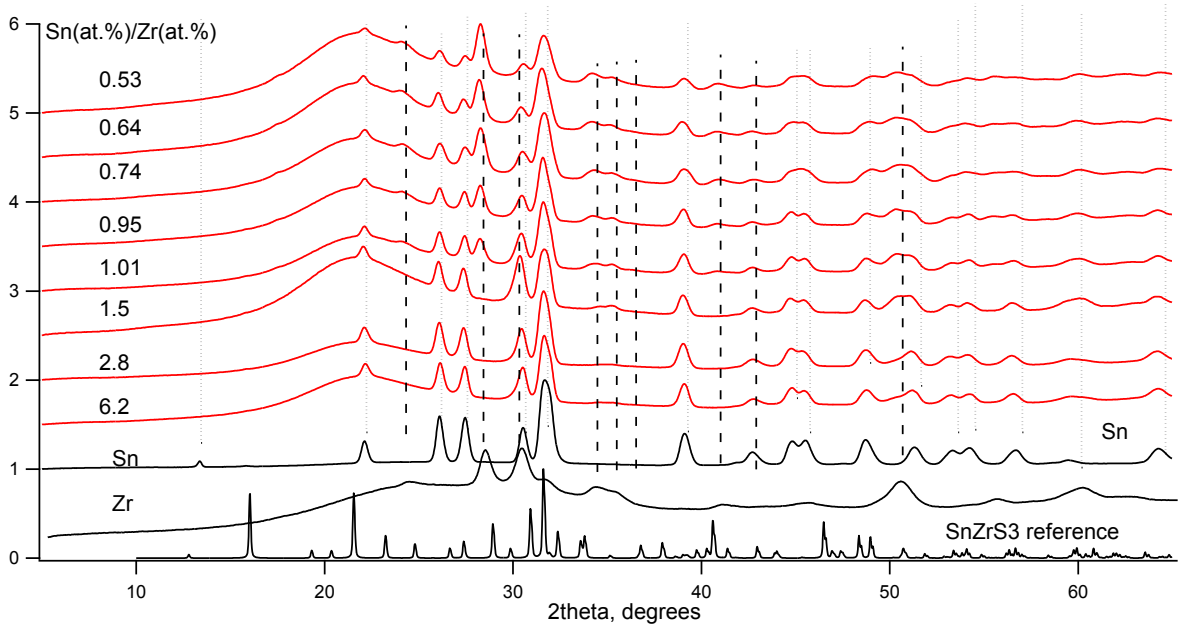

Fig. 16 XRD patterns of annealed Sn, Zr and Sn/Zr samples (Fig. 14), and reference $SnZrS_3$ pattern. Vertical dashed and dotted lines indicate positions of SnS and ZrO_2 peaks.

Sn/Zr, S/Zr and O/Zr ratios in the annealed samples are shown in Fig. 17 as a function of the anneal temperature. Sn/Zr ration changes with annealing temperature, which indicates that it would be challenging to obtain $SnZrS_3$ films by this method. Sn/S ratio in the annealed films is close to 1 for the samples annealed in 400-600 $_oC$ range, but it deviates from 1 above 600 ^oC. This may be attributed to a phase transition in SnS at 603 ^oC. For all the sample, O/Zr ratio is close to 2. The results of these experiments indicate that the mixed-phase sample of SnS and ZrO_2 is formed as a result of H_2S anneal. These results are consistent with the XRD patterns (Fig. 16)

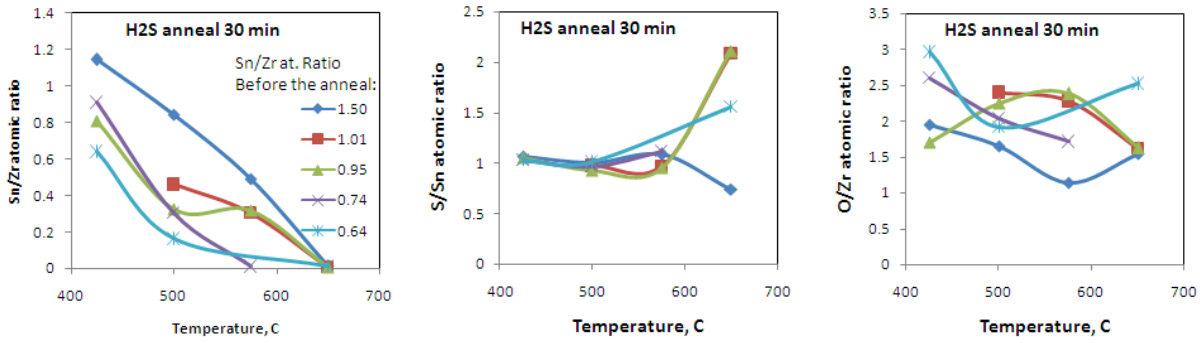

Fig. 17 Sn/Zr, S/Zr and O/Zr atomic ratios in the Sn/Zr multilayers sulfurized at different temperatures for 30 min.

Sn/Zr, S/Zr and O/Zr ratios in the annealed samples are shown in Fig. 18 as a function of the annealing dwell time. Data point at zero time indicate the atomic ratios in as-deposited samples. Sn/Zr atomic ratios change significantly after the anneal, and this change is more predictable for the sample with low starting Sn/Zr ratio. O/Zr ratio fluctuates around 2 and is also more predictable for the sample with low Sn/Zr starting ratios. S/Sn ratio stays 1 for all the anneal times.

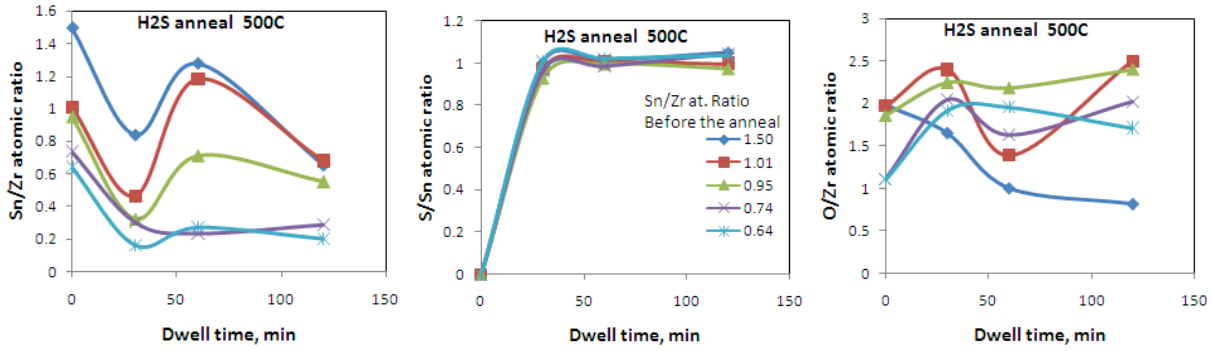

Fig. 18 Sn/Zr, S/Zr and O/Zr atomic ratios in the Sn/Zr multilayers sulfurized for different times at 500 ^{o}C

A brief study of the effects of the other parameters of the flowing gas process did not improve the composition and phase of the resulting samples. All the films contained Zr-O. Oxidation of the samples starts by getting in the PLD chamber, and completes during the H_2S anneal. High reactivity of the films with oxygen is attributed to the presence of Zr. Other reactive metals, such as Mg[8] and Ta[7] do not show this effect.

Possible solution to the problems of the described process is deposition of the metal multilayers in ultra-high vacuum and using long Zr preablation times for oxygen gettering in the chamber. Another route is to start with the multilayers of ZrS_2/SnS or ZrS_2/SnS_2. Both of these options in principle can be realized in the Thermionics chamber. However, on practice such process would be rather difficult, because at the present time Thermionics is not equipped with the automated target-switching mechanism.

Summary

The main result of this study is that the flowing gas anneal of the Sn/Zr multilayers is not a viable route to preparation of $SnZrCh_3$ thin films. The main reason for it is high reactivity of Zr with oxygen. The reaction starts in the PLD chamber (gettering) and completes in the flow furnace. Additional difficulties in the stoichiometry control are caused by loss of Sn in the anneal process.

Section 4. Thin films of binary chalcogenides in Sn-Zr-Ch system

Experiment

Zr-Se thin films were prepared by PLD on a-SiO_2 substrates heated to 600 and 700 ^oC substrate temperatures, 1 J/cm^2 laser beam intensity, 5 Hz repetition rate by performing 10000 laser pulses from a stoichiometric cold-pressed target made of $ZrSe_2$ powder synthesized in vacuum-sealed tubes. The targets strongly degassed when ablated in vacuum, so the pressure during raised PLD was up to 10^{-5} Torr.

Sn-S films were prepared from a SnS_2 target which had a brownish color. The films were deposited in 1 mTorr of Ar, using 1 J/cm^2 laser beam operating at 10 Hz; the target-substrate distance was kept at 2" and the substrate temperature was changed between 100 and 600 ^oC.

In addition to pure SnS thin films, SiO_2/ITO/BaCuChF/SnS/Al heterostructures were using 200-nm BaCuChF and 1000 nm SnS layers deposited on commercial SiO_2/ITO substrates heated to 400 ^oC. There was a ~5 sec interval between these two depositions. Al top-contact was deposited at room temperature.

Composition, structure, optical and transport properties of the films were studied by EPMA, XRD, absorption spectroscopy, resistivity and Seebeck effect measurements. The IV curves of the heterostructures were measured with a positive contact to ITO and negative contact to Al layers.

Results and discussion

A. Zr-Se films

It was found that the films prepared from the target processed in ambient lab atmosphere contain significant amount of ZrO_2 impurity. Therefore, the powder for the target was prepared by grinding Zr and Se instoichiometric proportions in Ar-filled glove bag.[1] When the careful care was taken to prevent oxidation during the powder synthesis and target production, the amount of crystalline ZrO_2 in the films was significantly reduced, but still remained detectable by XRD. (Fig. 19)

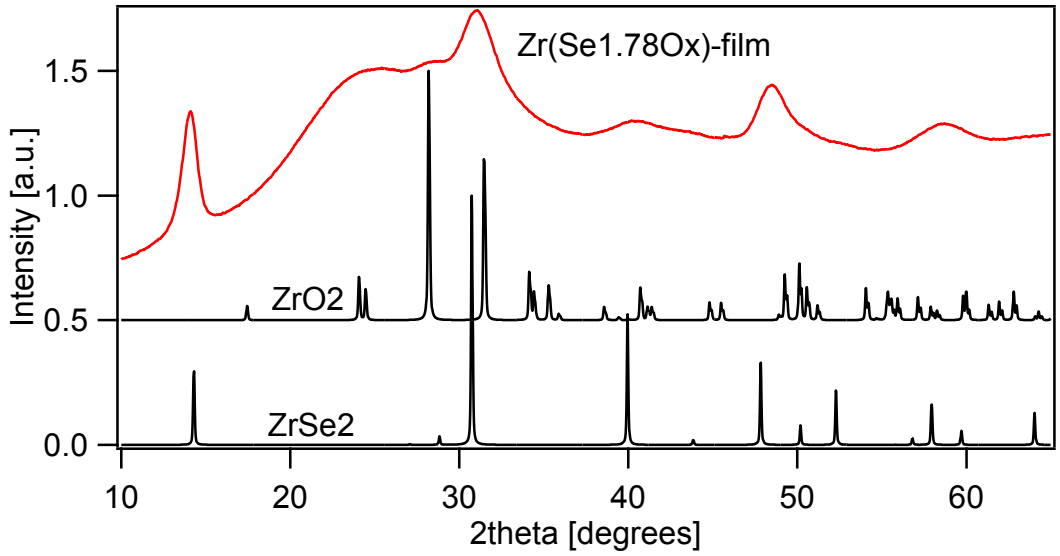

Fig. 19 XRD pattern of $ZrSe_2$ film deposited at 700 ^oC.

According to EPMA, Zr-Se films deposited at 600 and 700^oC film have Se/Zr ratio of 1.78, so Se vacancies must be present. The exact concentration of O could not be measured, because the film was deposited on a-SiO2, but it must be considerable, since ZrO2 XRD peaks were observed. Zr-

Se samples deposited at lower temperature (~400 ^{o}C) had larger deviation of Se from the stoichiometry and larger oxygen content. In addition, crystalline quality of $ZrSe_2$ phase was much lower at 400 ^{o}C.

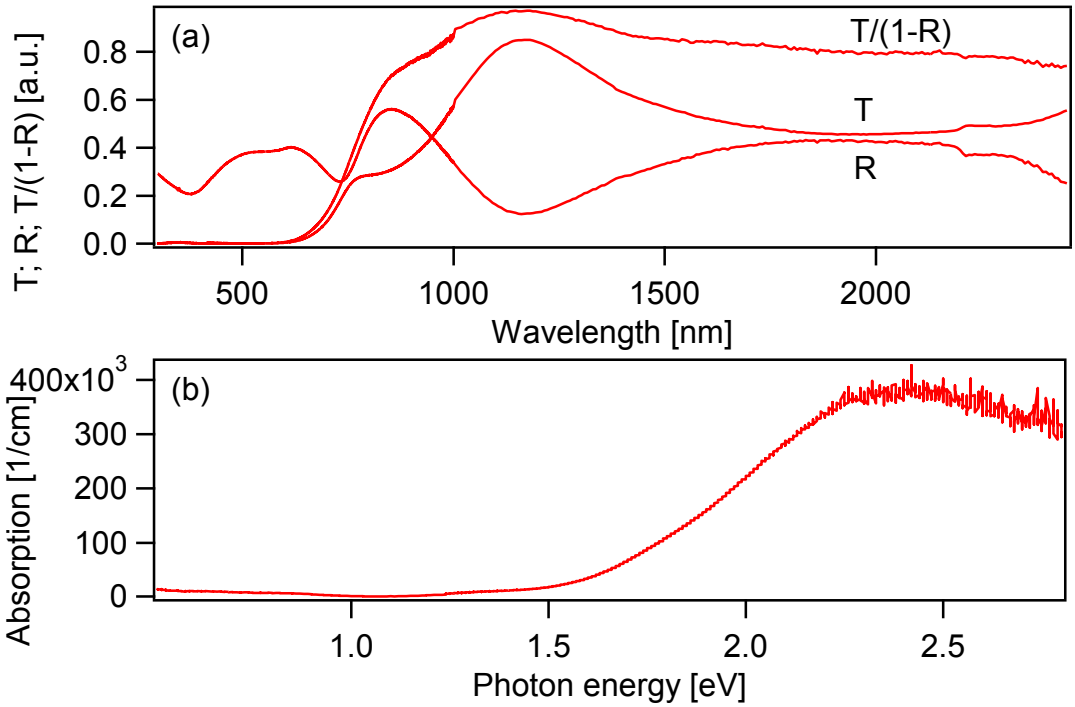

Fig. 20 Optical properties of $ZrSe_2$ thin films deposited at 700 ^{o}C.

Transport measurements indicate that the films deposited at 600 ^{o}C have *n*-type conduction which is consistent with the presence of Se vacancies. The resistivity of the samples is ~80 mOhm cm and the Seebeck coefficient is -214 μV/K. Hall coefficient of the film could not be reliably measured, most likely due to scattering of free charge carriers on the grain boundaries that contain ZrO_2 impurity, according to our XPS measurements on $ZrSe_2$ pellets.

Optical properties of Zr-Se film deposited at 700 ^{o}C are shown in Fig. 20. The film is transparent above 600 nm, so it looks dark-red to the eye. Thickness of 180 nm and refractive index of 2.73

(at 2000 nm) was determined from the interference pattern. Absorption coefficient starts to increase close to 1.5 eV. The optical band gaps determined from indirect and direct-bandgap analysis are 1.4 eV and 1.9 eV, respectively. The indirect band gap is higher than 1.2 eV, reported in the literature, which indicates that $ZrSe_{2-x}O_x$ is formed.

B. Sn-S films

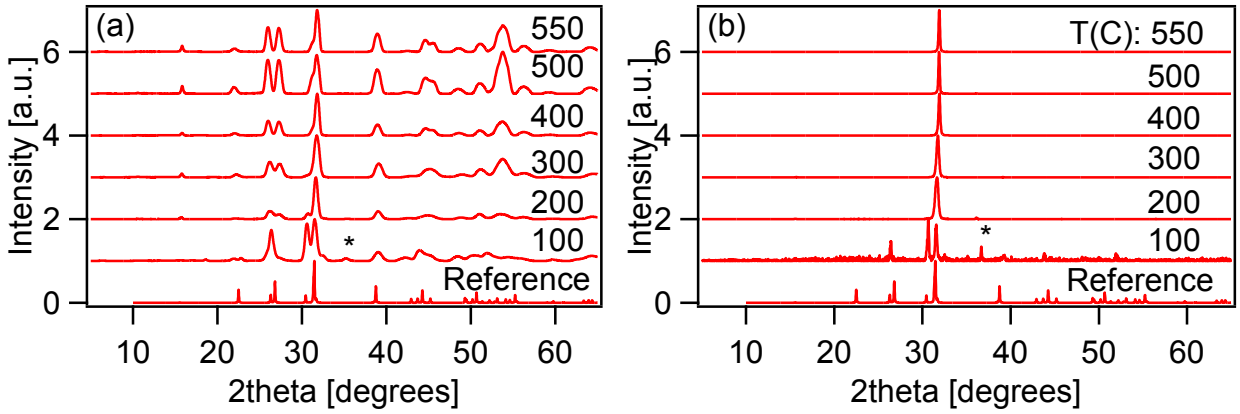

Fig. 21 XRD patterns of the SnS thin films measured using (a) Rigaku Rapid and (b) Rigaku Miniflex. SnS_2 peaks are indicated with stars

XRD pattern of Sn-S films prepared from SnS_2 target at different temperatures are shown in Fig. 21. XRD peaks of the films prepared at 200^{o}C and higher can be indexed to SnS Pnma structure. A weak SnS_2 peak is observed for the film deposited at 100 ^{o}C, and perhaps for the 200 ^{o}C-film, but only after the careful analysis using the log-scale plot. It is interesting to note that the deposition from the SnS_2 target in Ar atmosphere produces SnS films. Similar occurs for the deposition in UHV, so scattering on Ar must not be the reason for the loss of sulfur.

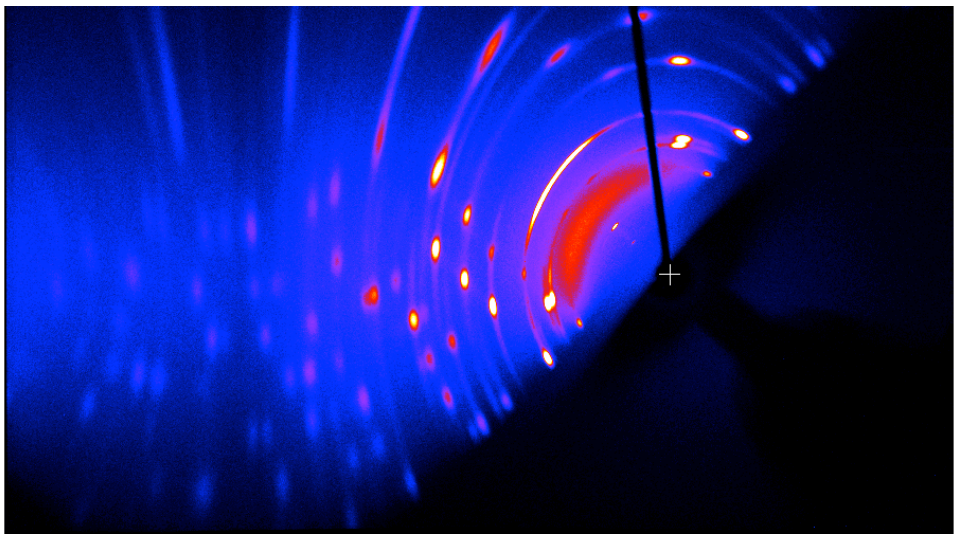

Fig. 22 Spatial intensity distribution of the x-rays diffracted of SnS film and collected using a cylindrical detector. The spots reveal preferential orientation of the SnS film deposited at 300^{o}C.

All the SnS films have preferred 111 orientation with small contribution of 002 and 004 orientations (Fig. 21b). In the XRD patterns measured using the Rapid, all the peaks appear in the I(2θ) plot due to cylindrical shape of the detector and due to rotation of the sample during the data collection, but texture can be shown using characteristic spots on the detector image (Fig. 22). As the substrate temperature increases, degree of the preferential orientation changes, with the maximum at ~300-500 ^{o}C. Above 550 ^{o}C, the film thickness starts to decrease and the grain size starts to increase, so the films start looking milky. At 600 ^{o}C and higher the films do not adhere to glass substrate. This correlates with the phase transition of SnS in this temperature range. It means that the high-temperature SnS phase is not stable under the PLD conditions.

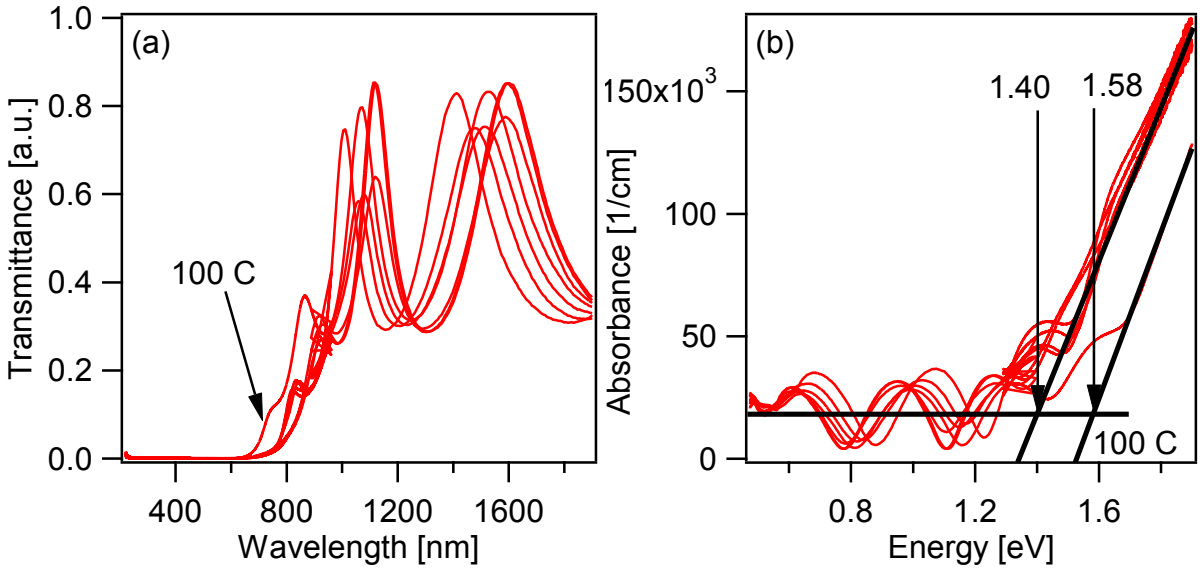

Fig. 23 (a) Transmittance and (b) absorbance of SnS thin films prepared at different substrate temperatures

Optical properties of the SnS films are shown in Fig. 23. The 400-nm films have 50% average transmittance above 1000 nm. The transmittance is low due to large reflectance, so the films must have large refractive index (Fig.23a). The reflectance interference fringes could not be matched with the transmittance fringes to give flat T/(1-R), so the absorbance was determined from transmittance only (Fig.23b) The SnS films have a strong absorption edge at 1.40 eV, and the film that contained SnS_2 impurity has the absorption edge at 1.58 eV. These absorption edges do not correspond to the lowest energy gap of SnS, because it is known that SnS is an indirect-band-gap semiconductor with ~1 eV band gap. A strong absorption edge at 1.4 eV makes SnS films suitable for photovoltaic applications.

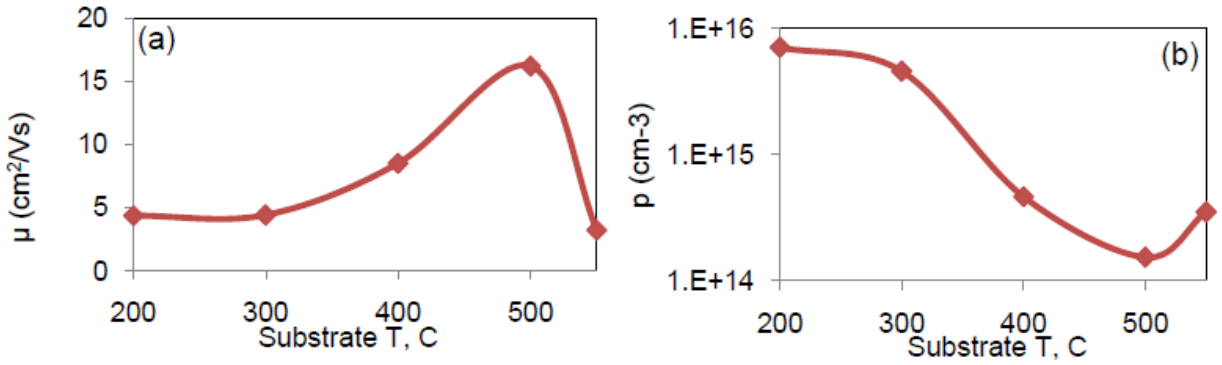

Fig. 24 (a) Mobility and (b) concentration of free holes in SnS films as a function of substrate temperature during the deposition.

Transport properties of SnS films change with the change of substrate temperature during the deposition. (Fig.24) As the substrate temperature increases, mobility of free holes increases from 5 to 15 cm^2/Vs, and their concentration decreases from 10^{16} to 10^{14} cm^{-3}. Both trends indicate increase of the film's structural quality with increasing substrate temperature. The mobility of the 550 ^oC film is small, perhaps due to poor film morphology.

SnS films are very attractive for doping studies, because introduction of any kind of dopand would most certainly lead to the change in the SnS transport properties. There is a report in literature on n-type conductivity in SnSe:Sb crystals.[9] If n-type conduction can be achieved, SnS p-n homojunction solar cell can be fabricated. If achieving n-type conductivity in SnS proves difficult, SnS/$ZrSe_2$ p-n junctions can be fabricated.

Low concentration of free mobile holes in undoped SnS films is also suitable for application of this materials as i-layer in p-i-n solar cells. Preliminary estimation of the band alignment leads to the conclusion that BaCuTeF and ZnS would be good candidates for the p-window and n-window layers, respectively. Therefore the proposed structure is

SiO_2/ITO/ZnS/SnS/BaCuTeF/Cu. ZnS is an insulating materials, therefore thin (~10 nm) ZnS layers should be used. Alternatively, Zn(OS) can be used as a n-window layer, because of its higher concentration of free electrons.[10] This layer can be deposited using ZnS target in Ar/O_2 atmosphere. The work on fabrication and characterization of the proposed p-i-n heterostructures is currently in progress.

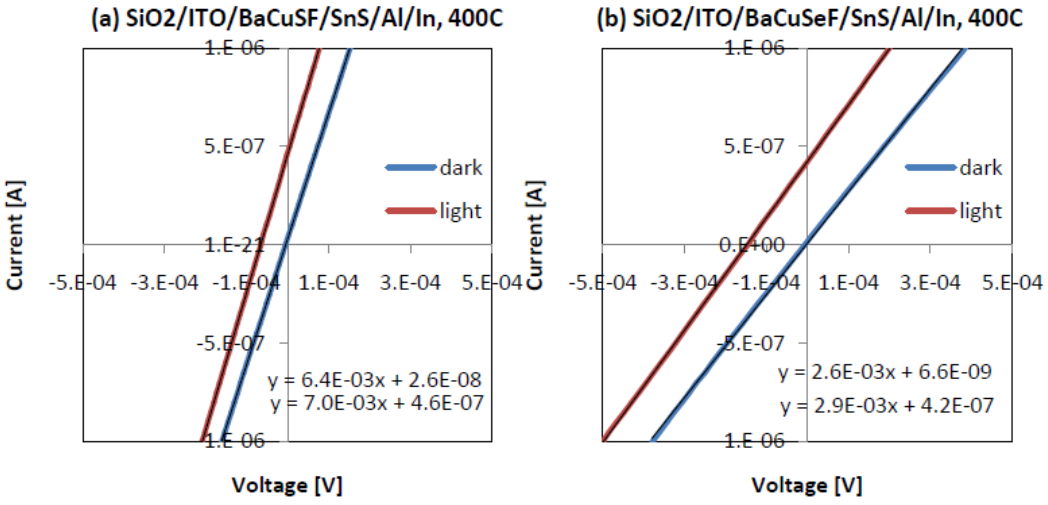

Fig. 25 I-V curves of the heterostructures in a dark room and under the table lamp illumination.

Current-voltage characteristic of the SiO2/ITO/BaCuChF/SnS/Al heterostructures are shown in Fig. 25 Negative sign of the open-circuit volage indicates that the photogeneration most likely happens at the ITO/BaCuChF interface. To some extent this is expected, since both BaCuChF and SnS are p-type semiconductors.

Summary

Zr-Se thin films were prepared by PLD. The optimal temperature for the deposition is 600-700^{o}C. Under these conditions, the samples are polycrystalline, the stoichiometry of the samples is close to $ZrSe_2$, and concentration of oxygen impurity is minimal. Zr-Se samples have an

absorption onset close to 1.5 eV and have refractive index of 2.73 at 2000 nm. The samples show n-type transport with the resistivity of 80 mOhm cm and a Seebeck coefficient of -214 μV/K. SnS films deposited from SnS_2 target show preferred (111) orientation, low 10^{14}-10^{16} cm^{-3} concentration of free mobile holes, and a strong absorption edge close to 1.4 eV. All these properties are favorable for the fabrication of p-i-n solar cells using this material.

---

[1] A. P. Richard, Ph.D. thesis, Oregon State University (2010)
[2] D. Harada, M.S. thesis, Oregon State University (2010)
[3] D. Johnson, private communication
[4] D. B. Chrisey and G. K. Hubler, *Pulsed Laser Deposition of Thin Films*, 1st ed. (Wiley-Interscience, 1994).
[5] S. A. Chambers, private communication
[6] H. Katagiri, K. Jimbo, S. Yamada, T. Kamimura, W. S. Maw, T. Fukano, T. Ito, and T. Motohiro, Appl. Phys. Express **1**, 041201 (2008).
[7] P. F. Newhouse, Ph.D. thesis, Oregon State University (2008)
[8] D. Keszler, private communication
[9] J. Umeda, J. Phys. Soc. Jpn. **16**, 124-125 (1961).
[10] C. Platzer-Bjorkman, T. Torndahl, D. Abou-Ras, J. Malmstrom, J. Kessler, and L. Stolt, J. Appl. Phys. **100**, 044506-9 (2006).